

Seasonal Water “Pump” in the Atmosphere of Mars: Vertical Transport to the Thermosphere

Dmitry S. Shaposhnikov^{1,2}, Alexander S. Medvedev³, Alexander V. Rodin^{1,2},
and Paul Hartogh³

¹Moscow Institute of Physics and Technology, Moscow, Russia

²Space Research Institute, Moscow, Russia

³Max Planck Institute for Solar System Research, Göttingen, Germany

Key Points:

- Global circulation modeling reveals the mechanism of water exchange between the lower and upper atmosphere
- Atmospheric dust controls the circulation strength and, hence, the amount of high-altitude water
- Solar tide modulates the upwelling of water vapor by almost completely shutting it down during certain local times

arXiv:1904.06391v1 [astro-ph.EP] 12 Apr 2019

Corresponding author: D. S. Shaposhnikov, shaposhnikov@phystech.edu

Abstract

We present results of simulations with the Max Planck Institute general circulation model (MPI–MGCM) implementing a hydrological cycle scheme. The simulations reveal a seasonal water “pump” mechanism responsible for the upward transport of water vapor. This mechanism occurs in high latitudes above 60° of the southern hemisphere at perihelion, when the upward branch of the meridional circulation is particularly strong. A combination of the mean vertical flux with variations induced by solar tides facilitates penetration of water across the “bottleneck” at approximately 60 km. The meridional circulation then transports water across the globe to the northern hemisphere. Since the intensity of the meridional cell is tightly controlled by airborne dust, the water abundance in the thermosphere strongly increases during dust storms.

1 Introduction

Water is a minor component of the Martian atmosphere, which is largely confined within a few lower scale heights. Nevertheless, it is the main source of hydrogen in the upper atmosphere [Hunten and McElroy, 1970; Parkinson and Hunten, 1972; Krasnopolsky, 2002]. Escape of hydrogen atoms into space near the exobase varies by an order of magnitude seasonally, maximizing around southern summer solstice (solar longitude $L_s \approx 270^\circ$), according to MAVEN [Halekas, 2017] and HST observations [Bhattacharyya et al., 2017] during dust storms [e.g., Bhattacharyya et al., 2015; Chaffin et al., 2014; Clarke et al., 2014, 2017]. Observed water in the lower atmosphere also experiences strong seasonal changes and depends on airborne dust load [e.g., Smith et al., 2009; Maltagliati et al., 2011a; Trokhimovskiy et al., 2015; Pottier et al., 2017]. This implies a link between water in the troposphere and thermosphere and a corresponding mechanism of transport between the layers.

The Martian middle atmosphere is too cold to sustain water vapor, especially around the mesopause, while ice particles are sufficiently heavy and prone to sedimentation. This water behavior is similar to that in the terrestrial middle atmosphere [Seele and Hartogh, 1999]. However, there are multiple observations showing a presence of water vapor in the middle atmosphere at certain locations and times [e.g., Maltagliati et al., 2013; Fedorova et al., 2018]. Heavens et al. [2018] and Fedorova et al. [2018] provided evidence of strong seasonal variations of the globally averaged water abundance and its vertical extension up to 70–80 km at perihelion during the Martian Year 28 (MY28) global dust storm. Hypotheses concerning the mechanism of vertical transport of water include mesoscale deep convection [Heavens et al., 2018], turbulent mixing in the lower atmosphere and/or an unspecified dynamics in the upper atmosphere [Clarke, 2018]. General circulation modeling underestimates the hygropause altitude at southern summer solstice to date [Chaufray et al., 2015; Pottier et al., 2017].

Our study addresses this gap in knowledge of processes that couple water in the lower and upper atmosphere. We present results of simulations with our recently developed hydrological scheme [Shaposhnikov et al., 2018a] implemented in the Max Planck Institute Martian general circulation model (MPI–MGCM). This is the first modeling study that considers in detail the transport of water from the surface to the thermosphere and explores its dependence on dust storms. In section 2, we outline the modeling tools and setup of numerical experiments. The annual cycle of vertical water transport is discussed in Section 3. In sections 4 and 6, we zoom in on the perihelion season and explore the zonal mean transport of water and local time variations, correspondingly. The results of simulations are compared with observations from Mars Climate Sounder onboard Mars Reconnaissance Orbiter (MCS–MRO) in section 7.

2 Model description and Design of Simulations

The MPI-MGCM has been described in detail in the papers of *Hartogh et al.* [2005, 2007]; *Medvedev and Hartogh* [2007]. It employs a spectral dynamical solver for the primitive equations of hydrodynamics on a sphere. In the vertical, the grid is discretized by 67 hybrid η -levels, terrain-following near the surface and pressure based near the top at 3.6×10^{-6} Pa (~ 160 km). The model includes a set of physical parameterizations suitable for the Martian atmosphere from the ground to the thermosphere. T21 horizontal resolution (corresponding to $\approx 5.6^\circ$) was used in the simulations. Subgrid-scale gravity waves were parameterized as described in the work of *Medvedev et al.* [2011a].

The hydrological part of the model has been described in detail in the papers of *Shaposhnikov et al.* [2016, 2018a]. It includes a semi-Lagrangian transport of water vapor and ice, and accounts for the microphysics of vapor-ice conversions. Ice clouds are formed whenever water vapor condenses on cloud condensation nuclei (CCN). The heterogeneous nucleation rate and ice particle growth rate are evaluated according to *Jacobson* [2005]. The sizes of CCN are represented by four bins. A two-moment scheme is applied to every bin for separately keeping track of the ice mass and number of particles [*Rodin*, 2002]. The size of ice particles determines their microphysical properties and the sedimentation rate. The CCN number density in each bin is calculated from the bimodal log-normal dust distribution [*Fedorova et al.*, 2014], as described in the paper of *Shaposhnikov et al.* [2018a, section 2.2].

Unlike with our previous simulations of the water cycle [*Shaposhnikov et al.*, 2018a], those presented here have been performed in the domain extending into the thermosphere, where water is no longer chemically conservative and accurate photochemical modeling may have to be included depending on the motive [e.g., *Hartogh et al.*, 2010]. For purposes of this work, we retained only a parameterization of H_2O losses due to photodissociation. The water photodissociation rates have been calculated according to *Anbar et al.* [1993, formulae (1)–(2)].

In this study we employ two predetermined dust scenarios. The “basic” one represents an observationally-based seasonally and latitudinally evolving (i.e., zonally averaged) aerosol optical depth τ in the thermal IR based on MGS-TES and MEX-PFS measurements with the global dust storms removed [*Medvedev et al.*, 2011a]. The second one is based on the measurements for the Martian Year 28 (MY28), which included a major dust storm during the perihelion season [*Medvedev et al.*, 2013, Figure 3]. In both scenarios, vertical profiles of dust were prescribed after *Conrath* [1975] with modifications described in the paper of *Medvedev et al.* [2013, Formulae 1 and 2].

The model has been initialized with the distribution of water vapor and ice obtained in our earlier simulations [*Shaposhnikov et al.*, 2018a]. The latter runs have been performed for several Martian years until the model achieved a quasi-stable state. Since the current version of the MGCM extends higher into the thermosphere, the additional vertical levels have been initialized with the values at ~ 100 km. The initial conditions for the dynamical fields are taken from the simulations of *Medvedev et al.* [2016].

The total amount of water in the atmosphere depends on the model time step due to the instability of commonly used nucleation and particle growth schemes [*Navarro et al.*, 2014; *Shaposhnikov et al.*, 2018a, see the discussion around Figure 11]. Therefore, we applied a 10 s time step for microphysics and other model processes in order to suppress instabilities and increase accuracy.

3 Vertical Transport of Water Vapor

Vertical transport of water vapor and ice is best characterized by the corresponding fluxes. Figure 1 presents latitude-seasonal distributions of the vertical water vapor flux at several altitudes simulated using the “basic” dust scenario. It clearly shows that at all altitudes above 30 km, the flux maximizes around perihelion between $L_s = 200^\circ$ and 300° (Figure 1b-f) and is negligibly small throughout the rest of the year. The flux distributions are approximately symmetric with respect to the solar longitude $L_s = 260^\circ$, when the global mean temperature reaches its annual maximum. Between $L_s = 220^\circ$ and 300° , the transport of water vapor up to ~ 90 km follows the meridional circulation cell with air rising in the summer hemisphere and sinking in the winter one. In the thermosphere above 120 km, the distributions indicate additional circulation cells in low-to-middle latitudes. However, the pole-to-pole transport persists, and the magnitudes of upward and downward fluxes over the, correspondingly, southern (summer) and winter (northern) poles significantly increase.

The other thing that stands out in Figure 1c is the ~ 2 ppmv m s^{-1} minimum of the upward water flux at perihelion located at around 60 km. This is the only region (between 20°S and 70°S) where at certain times of the year water can penetrate from the lower atmosphere into the upper layers. Once water is through this “bottleneck”, it is transported further upward and across latitudes northward. Note that not all the water stays in the upper atmosphere with the prospect of being photolyzed and ultimately escaping to space. The global circulation also returns a portion of water to the lower atmosphere in the northern polar region, as is shown with bluish shades in Figure 1c.

4 Water Transport at Perihelion

We next zoom in on the perihelion season and consider the water transport in more detail. Figure 2a presents the water vapor amount in ppmv averaged diurnally and between $L_s=250^\circ$ and 270° . Streamlines show the residual meridional circulation, while their thickness and color indicate the magnitude and vertical direction of the water vapor flux, correspondingly. In agreement with previous observations and simulations, it is seen that the dominant part of water vapor concentrates in the southern (summer) hemisphere below ~ 45 km. Water increasingly sublimates near the surface at middle to high latitudes and is transported up- and northward by the meridional cell. This results in the water vapor maximum of up to a few hundred ppmv at around 30 km that extends in latitude to $\sim 45^\circ\text{N}$. Water ice clouds (shown with white contours) form immediately above and are transported by the meridional circulation in the same manner as vapor. Color shades in Figure 2a demonstrate an elevated amount of water vapor (~ 90 – 140 ppmv) in the high-latitude “bottleneck” between ~ 60 and 90 km. Higher up at around the mesopause and in the lower thermosphere (see Figure 2c), the water vapor is effectively transported across the globe by the meridional circulation, and its magnitude increases up to ~ 160 ppmv (in the average sense mentioned above).

Thick contour lines in Figure 2a demonstrate a strong downward flux of vapor in the north polar region at all altitudes in the middle and upper atmosphere. As a consequence, the water vapor mixing ratio increases there as well. Note that the same water mass produces larger volume mixing ratio in the upper atmosphere due to exponentially decaying pressure and density. This downwelling over the winter pole is the major mechanism of returning water back to the lower atmosphere. Due to colder temperature and higher pressure, this water condenses and contributes to the ice polar hood at around 30 km (depicted by the white contour lines). Unlike molecular diffusion, which prevents accumulation of water in the upper atmosphere at all latitudes and times, this mechanism is distinctively seasonal and localized.

5 Water During Dust Storm

After illustrating the mechanism of lifting water vapor up through the “bottle-neck”, we turn our attention to the causal relationship between the high-altitude water and atmospheric dust. There are several channels, through which the former can affect the latter. Absorption of solar radiation by airborne aerosol increases temperature and, thus, hinders condensation of water. On the other hand, the increasing number of particle nuclei facilitates formation of ice clouds. Finally, dust storms strongly amplify the meridional circulation [e.g., *Medvedev et al.*, 2011b].

We repeated the simulations with the dust scenario based on column opacity measurements during MY28 when a major planet-encircling dust storm occurred around the season of interest. For simplicity, we use the direct model output of water vapor rather than applying the indirect method of *Heavens et al.* [2018] to the model temperature and water ice fields. Figure 2d shows that temperature increased by ~ 20 K over the south pole and by more than 30 K over the north pole at 45 km (see color contours for temperature differences with the “basic” dust scenario). The meridional transport intensified during the dust storm. In particular, the warming over the winter pole is caused adiabatically by the downward branch of the circulation cell [e.g., *Hartogh et al.*, 2007; *Kuroda et al.*, 2009]. The changes in temperature and transport remarkably affected atmospheric water. Thus, the total amount of water vapor in the atmosphere noticeably increased (see Figure 2b) and its upper boundary (hygropause) extended above ~ 60 km, ~ 10 km higher than in the “basic” dust scenario. Correspondingly, the simulated ice clouds became denser, and their top has elevated by ~ 10 km in the southern hemisphere. The enhancement of the circulation is the global phenomenon that covers altitudes up to the thermosphere. Consequently, the vertical transport of water vapor increases in the southern hemisphere as well, which is depicted by thicker contour lines in Figure 2b. This produced a maximum of water vapor of up to 220 ppmv between 120 and 150 km at 30°S – 90°S . Somewhat warmer temperatures in low to middle latitudes in the mesosphere and thermosphere during the dust storm (see color contours in Figure 2d) along with the enhanced transport produced increased vapor abundances at all heights above ~ 70 km. It is seen that there are fewer “dry” regions in the middle atmosphere compared to those for the “basic” dust simulation. Finally, the simulation reproduces the change in water vapor abundance in the south observed by *Fedorova et al.* [2018] but seems to underestimate water vapor at 60–75 km in the tropics and northern extratropics (as observed by both *Fedorova et al.* [2018] and *Heavens et al.* [2018]).

Another effect of the dust storm captured by the model is the increase of CCN in the atmosphere. A larger number of nuclei aids water vapor condensation, the formed ice particles have smaller radii and, thus, slower sedimentation speed. Therefore, water ice clouds form higher, which too contributes to increased water abundances in the upper atmosphere.

We illustrated that an increase of the airborne dust “widens” up the “bottleneck” for water penetration into the upper atmosphere in the high-latitude southern hemisphere both dynamically and microphysically. The above consideration was based on the mean (diurnally/zonally averaged) fields. In the next section, we turn our attention to local time variations.

6 Local Time Variations

Figure 3 shows deviations of the water vapor abundance (shaded) and vertical velocity (contours) from the corresponding zonal mean quantities as a function of local time in a particular grid point close to the south pole (75°S , 0°E). This composite plot is based on multi-day averaging over the period between $L_s = 250^\circ$ and 270° . It is

seen from Figure 3a for the “basic” dust scenario that the vertical velocity exhibits a mixture of the diurnal and semidiurnal tides with phase advancing with height. The downward phase tilt is the manifestation of the tide generated below and propagating upward. The angle of the tilt progressively changes with altitude above ~ 70 km to almost vertical, indicating the increasing role of the in situ-excited tides in the upper atmosphere. Note that our results are shown for high latitudes of the summer hemisphere (above 75°S), whereas modeling [e.g., *Forbes and Miyahara, 2006*] and MCS–MRO observations [*Kleinböhl et al., 2013*] provide evidence that the amplitude of the semidiurnal temperature variations maximizes in middle- to high latitudes of the winter hemisphere. There is no contradiction in that, because tide is a global phenomenon, in which amplitudes of fluctuations of different field variables can peak at different latitudes [e.g., *Yiğit and Medvedev, 2017*].

Unlike the vertical velocity, water vapor varies mainly with the diurnal periodicity with the maximum magnitude of ~ 120 ppmv at 30 km. Interactions with the semidiurnally varying vertical velocity form a characteristic steep reversal of water anomalies at 40 km by pushing water up and down twice per day [cf. to Earth, *Hallgren and Hartogh, 2012*]. The magnitude of the diurnal variations of water vapor at the “bottleneck” altitude around 60 km is 30–50 ppmv. Given that the mean vapor abundance in this region is around 70 ppmv, the total amount varies considerably with more water during the first half of a day. Higher in the middle and upper atmosphere, temporal variations of vapor are smaller, but correlate more with the upward fluxes. The major dust storm contributes to formation of giant diurnal water vapor variations in the lower atmosphere of greater than 500 ppmv at 30–40 km (Figure 3b). They occur due to enhanced sublimation from the reservoir on/under the surface. The variations extend higher into the middle atmosphere with the magnitude of ~ 100 –150 ppmv at the “bottleneck” around 60 km. A comparison with the zonal mean values in Figure 2b shows that some “leakage” of vapor into the middle and upper atmosphere takes place also during the second half of day in addition to strong tidally-modulated pulses during the first half. Above the mesopause, the semidiurnal tide weakens during the dust storm, and its correlation with the water vapor amount becomes less certain.

7 Comparison With MCS Observations

In order to validate our simulations, we compare them with the data inferred from the measurements by the MCS–MRO during MY28 [*Heavens et al., 2018*]. The authors of the latter study used an indirect method to estimate the water vapor and ice abundances from the observations of temperature and water ice clouds. MCS performs 13 polar orbits per Martian sol. Away from the poles, the groundtrack of MRO corresponds to approximately 15:00 hours local solar time on the ascending side of the orbit (Figure 4a) and to ~ 3 :00 local time on the opposite side (Figure 4c). Since MCS orbits vary, we used the model output averaged over the intervals 14:00–16:00 and 2:00–4:00 hours local time for comparison, correspondingly. Both observations and modeling in Figure 4 show gradual, but rapid increase of the total water abundance and its rise in altitude towards the perihelion season. There were no successful retrievals available during the dust storm itself between approximately $L_s = 260^\circ$ and 305° and above 80 km. However, at the highest available levels between 70 and 80 km, both the model and observations agree well in showing ~ 70 –80 ppmv of water. Good agreement also exists with the night-time measurements at 40–50 km immediately before the onset of the dust storm ($L_s = 220^\circ$ to 260°). Greater water abundances during the night time at these altitudes are due to the tidal phase (higher temperature), as can be seen from Figure 3b. Note that the MCS measurements demonstrate that the maxima of water are vertically localized around 40–50 km between $L_s = 200^\circ$ and 250° , whereas in the model the water mixing ratio increases down to the surface. This difference may be due to the adopted dust scenario that does not capture detached dust layers.

The model also demonstrates a rapid fall of water abundances after $L_s = 330^\circ$, which is not supported by the observations.

Nevertheless, the total observed and simulated amount of water during the dust storm as well as the shape of the seasonal distribution agree well, at least in the latitudinally averaged sense presented here. They clearly illustrate that conditions for upward water penetration across the “bottleneck” at ~ 60 km exist only during a limited time of the year around perihelion, and dust storms strongly enhance this penetration.

8 Discussion and Conclusions

Several mechanisms have been proposed to explain the observed presence of water in the middle atmosphere of Mars above 60 km. *Maltagliati et al.* [2011b] suggested supersaturation of water vapor due to purely microphysical reasons (lack of condensation nuclei). *Clarke* [2018] considered the dynamics and hypothesized that either turbulent mixing in the lower atmosphere raises water vapor upward, or the strengthened by solar UV circulation in the upper atmosphere facilitates this transport. *Heavens et al.* [2018] attributed the appearance of water vapor and ice at upper levels to deep convection enhanced dust storms. Our simulations with the general circulation model revealed the full picture of water transport from the ground up to the thermosphere. The main findings are the following.

- Water is lifted up in high latitudes of the summer hemisphere by the upward branch of the pole-to-pole meridional circulation cell. It is then transported by the latter across latitudes in the mesosphere and thermosphere.
- Water can penetrate upper levels only during the perihelion season, when the meridional circulation cell is sufficiently strong.
- The influx of water to the middle and upper atmosphere increases, whenever the meridional cell intensifies, for instance, during dust storms. In addition, dust storm-induced heating increases the amount of water vapor in the lower atmosphere.
- Upward transport of water is significantly modulated by the solar tide. The latter acts as a “pump” by increasing the transport during certain local times and almost completely shutting it down during the others.

The described transport of water to the Martian upper atmosphere has some similarities and differences with that on Earth. In the terrestrial stratosphere and mesosphere, there is also a strong water upwelling in the summer hemisphere that even compensates for photochemical destruction [*Hartogh et al.*, 2010]. Due to the circular orbit and unlike on Mars, it occurs during both solstices. However, water in the terrestrial atmosphere is rapidly destroyed by photolysis in the sun-lit summer hemisphere below 70 km, whereas on Mars its significant portion can be transported across the globe.

Photochemical calculations [*Chaffin et al.*, 2017; *Krasnopolsky*, 2019] suggest that water abundances of ~ 80 ppmv at 60–80 km can explain the observed magnitudes of hydrogen escape at the exobase. Our simulations show that, even at dustless seasons, the circulation can deliver these amounts of water over the southern high latitudes, at least during certain local times. Moreover, comparable abundances of vapor are distributed by the circulation over all latitudes above ~ 120 km. During major dust storms (similar to that of MY28), the corresponding water abundances increase by a factor 2 and more. Overall, our simulations at least partly reconcile the existing observations and estimates, reveal the impact of planetary-scale circulations on the behavior of water in the middle and upper atmosphere, and provide testable predictions for evaluating alternative hypotheses against future observations.

Acknowledgments

The data supporting the MPI-MGCM simulations can be found at <https://mars.mipt.ru>, <https://zenodo.org/record/1553514> [Shaposhnikov *et al.*, 2018b] or obtained from D. Shaposhnikov (shaposhnikov@phystech.edu).

The authors thank Anna A. Fedorova, Takeshi Kuroda and Nicholas Heavens for assistance with the observational data and helpful discussions. This work has been performed at the Laboratory of Applied Infrared Spectroscopy of Moscow Institute of Physics and Technology and at Max Planck Institute for Solar System Research. The work was partially supported by the Russian Science Foundation grant 16-12-10559 and German Science Foundation (DFG) grant HA3261/8-1.

References

- Anbar, A., M. Allen, and H. Nair (1993), Photodissociation in the atmosphere of mars: Impact of high resolution, temperature-dependent CO₂ cross-section measurements, *Journal of Geophysical Research: Planets*, *98*(E6), 10,925–10,931.
- Bhattacharyya, D., J. T. Clarke, J.-L. Bertaux, J.-Y. Chaufray, and M. Mayyasi (2015), A strong seasonal dependence in the Martian hydrogen exosphere, *Geophysical Research Letters*, *42*(20), 8678–8685.
- Bhattacharyya, D., J. Clarke, J.-Y. Chaufray, M. Mayyasi, J.-L. Bertaux, M. Chaffin, N. Schneider, and G. Villanueva (2017), Seasonal changes in hydrogen escape from Mars through analysis of HST observations of the Martian exosphere near perihelion, *Journal of Geophysical Research: Space Physics*, *122*(11).
- Chaffin, M., J. Deighan, N. Schneider, and A. Stewart (2017), Elevated atmospheric escape of atomic hydrogen from Mars induced by high-altitude water, *Nature Geoscience*, *10*(3), 174.
- Chaffin, M. S., J.-Y. Chaufray, I. Stewart, F. Montmessin, N. M. Schneider, and J.-L. Bertaux (2014), Unexpected variability of Martian hydrogen escape, *Geophysical Research Letters*, *41*(2), 314–320.
- Chaufray, J.-Y., F. Gonzalez-Galindo, F. Forget, M. Lopez-Valverde, F. Leblanc, R. Modolo, and S. Hess (2015), Variability of the hydrogen in the Martian upper atmosphere as simulated by a 3d atmosphere-exosphere coupling, *Icarus*, *245*, 282 – 294, doi:10.1016/j.icarus.2014.08.038.
- Clarke, J. T. (2018), Dust-enhanced water escape, *Nature Astronomy*, *2*(2), 114.
- Clarke, J. T., J.-L. Bertaux, J.-Y. Chaufray, G. R. Gladstone, E. Quémerais, J. Wilson, and D. Bhattacharyya (2014), A rapid decrease of the hydrogen corona of Mars, *Geophysical Research Letters*, *41*(22), 8013–8020.
- Clarke, J. T., M. Mayyasi, D. Bhattacharyya, N. M. Schneider, W. E. McClintock, J. I. Deighan, A. I. F. Stewart, J.-Y. Chaufray, M. S. Chaffin, S. K. Jain, A. Stiepen, M. Crismani, G. M. Holsclaw, F. Montmessin, and B. M. Jakosky (2017), Variability of D and H in the Martian upper atmosphere observed with the Maven IUVs Echelle channel, *Journal of Geophysical Research: Space Physics*, *122*(2), 2336–2344, doi: 10.1002/2016JA023479.
- Conrath, B. J. (1975), Thermal structure of the Martian atmosphere during the dissipation of the dust storm of 1971, *Icarus*, *24*, 36–46.
- Fedorova, A., J.-L. Bertaux, D. Betsis, F. Montmessin, O. Korablev, L. Maltagliati, and J. Clarke (2018), Water vapor in the middle atmosphere of Mars during the 2007 global dust storm, *Icarus*, *300*, 440–457.
- Fedorova, A. A., F. Montmessin, A. V. Rodin, O. I. Korablev, A. Määttänen, L. Maltagliati, and J. L. Bertaux (2014), Evidence for a bimodal size distribution for the suspended aerosol particles on Mars, *Icarus*, *231*, 239–260, doi: 10.1016/j.icarus.2013.12.015.

- Forbes, J. M., and S. Miyahara (2006), Solar semidiurnal tide in the dusty atmosphere of Mars, *Journal of the Atmospheric Sciences*, *63*(7), 1798–1817, doi:10.1175/jas3718.1.
- Halekas, J. (2017), Seasonal variability of the hydrogen exosphere of Mars, *Journal of Geophysical Research: Planets*, *122*(5), 901–911.
- Hallgren, K., and P. Hartogh (2012), First detection of tidal behaviour in polar mesospheric water vapour by ground based microwave spectroscopy, *Atmospheric Chemistry and Physics*, *12*(8), 3753–3759, doi:10.5194/acp-12-3753-2012.
- Hartogh, P., A. S. Medvedev, T. Kuroda, R. Saito, G. Villanueva, A. G. Feofilov, A. A. Kutepov, and U. Berger (2005), Description and climatology of a new general circulation model of the Martian atmosphere, *Journal of Geophysical Research*, *110*(E11), E11,008, doi:10.1029/2005JE002498.
- Hartogh, P., A. S. Medvedev, and C. Jarchow (2007), Middle atmosphere polar warmings on Mars: Simulations and study on the validation with sub-millimeter observations, *Planetary and Space Science*, *55*(9), 1103–1112, doi:10.1016/j.pss.2006.11.018.
- Hartogh, P., G. R. Sonnemann, M. Grygalashvyly, L. Song, U. Berger, and F.-J. Lübken (2010), Water vapor measurements at alomar over a solar cycle compared with model calculations by Lima, *Journal of Geophysical Research: Atmospheres*, *115*(D1), doi:10.1029/2009JD012364.
- Heavens, N. G., A. Kleinböhl, M. S. Chaffin, J. S. Halekas, D. M. Kass, P. O. Hayne, D. J. McCleese, S. Piqueux, J. H. Shirley, and J. T. Schofield (2018), Hydrogen escape from Mars enhanced by deep convection in dust storms, *Nature Astronomy*, *2*(2), 126.
- Hunten, D., and M. McElroy (1970), Production and escape of hydrogen on Mars, *Journal of Geophysical Research*, *75*(31), 5989–6001.
- Jacobson, M. Z. (2005), *Fundamentals of Atmospheric Modeling*, Cambridge University Press, Cambridge, UK.
- Kleinböhl, A., R. John Wilson, D. Kass, J. T. Schofield, and D. J. McCleese (2013), The semidiurnal tide in the middle atmosphere of Mars, *Geophysical Research Letters*, *40*(10), 1952–1959, doi:10.1002/grl.50497.
- Korablev, O., V. A. Krasnopolsky, A. V. Rodin, and E. Chassefière (1993), Vertical structure of Martian dust measured by solar infrared occultations from the Phobos spacecraft, *Icarus*, *102*(1), 76–87, doi:10.1006/icar.1993.1033.
- Krasnopolsky, V. A. (2002), Mars’ upper atmosphere and ionosphere at low, medium, and high solar activities: Implications for evolution of water, *Journal of Geophysical Research: Planets*, *107*(E12), 11–1.
- Krasnopolsky, V. A. (2019), Photochemistry of water in the Martian thermosphere and its effect on hydrogen escape, *Icarus*, *321*, 62 – 70, doi:10.1016/j.icarus.2018.10.033.
- Kuroda, T., A. S. Medvedev, P. Hartogh, and M. Takahashi (2009), On forcing the winter polar warmings in the Martian middle atmosphere during dust storms, *Journal of the Meteorological Society of Japan. Ser. II*, *87*(5), 913–921, doi:10.2151/jmsj.87.913.
- Maltagliati, L., D. V. Titov, T. Encrenaz, R. Melchiorri, F. Forget, H. U. Keller, and J. P. Bibring (2011a), Annual survey of water vapor behavior from the OMEGA mapping spectrometer onboard Mars Express, *Icarus*, *213*(2), 480–495, doi:10.1016/j.icarus.2011.03.030.
- Maltagliati, L., F. Montmessin, A. Fedorova, O. Korablev, F. Forget, and J.-L. Bertaux (2011b), Evidence of water vapor in excess of saturation in the atmosphere of Mars, *Science*, *333*(6051), 1868–1871.
- Maltagliati, L., F. Montmessin, O. Korablev, A. Fedorova, F. Forget, A. Määttänen, F. Lefèvre, and J.-L. Bertaux (2013), Annual survey of water vapor vertical distribution and water–aerosol coupling in the Martian atmosphere observed by SPICAM/MEX solar occultations, *Icarus*, *223*(2), 942–962.

- Medvedev, A. S., and P. Hartogh (2007), Winter polar warmings and the meridional transport on Mars simulated with a general circulation model, *Icarus*, *186*(1), 97–110, doi:10.1016/j.icarus.2006.08.020.
- Medvedev, A. S., E. Yiğit, P. Hartogh, and E. Becker (2011a), Influence of gravity waves on the Martian atmosphere: General circulation modeling, *Journal of Geophysical Research: Planets*, *116*(E10), doi:10.1029/2011JE003848.
- Medvedev, A. S., T. Kuroda, and P. Hartogh (2011b), Influence of dust on the dynamics of the Martian atmosphere above the first scale height, *Aeolian Research*, *3*(2), 145 – 156, doi:10.1016/j.aeolia.2011.05.001.
- Medvedev, A. S., E. Yiğit, T. Kuroda, and P. Hartogh (2013), General circulation modeling of the Martian upper atmosphere during global dust storms, *Journal of Geophysical Research: Planets*, *118*(10), 2234–2246.
- Medvedev, A. S., H. Nakagawa, C. Mockel, E. Yiğit, T. Kuroda, P. Hartogh, K. Terada, N. Terada, K. Seki, N. M. Schneider, S. K. Jain, J. S. Evans, J. I. Deighan, W. E. McClintock, D. Lo, and B. M. Jakosky (2016), Comparison of the Martian thermospheric density and temperature from IUVS/MAVEN data and general circulation modeling, *Geophysical Research Letters*, *43*(7), 3095–3104, doi:10.1002/2016GL068388.
- Montmessin, F., F. Forget, P. Rannou, M. Cabane, and R. M. Haberle (2004), Origin and role of water ice clouds in the Martian water cycle as inferred from a general circulation model, *J. Geophys. Res.*, *109*(E10004), 1–26, doi:10.1029/2004JE002284.
- Navarro, T., J.-B. Madeleine, F. Forget, A. Spiga, E. Millour, F. Montmessin, and A. Määttänen (2014), Global climate modeling of the Martian water cycle with improved microphysics and radiatively active water ice clouds, *Journal of Geophysical Research: Planets*, *119*(7), 1479–1495.
- Parkinson, T., and D. Hunten (1972), Spectroscopy and acronomy of o₂ on mars, *Journal of the Atmospheric Sciences*, *29*(7), 1380–1390.
- Pottier, A., F. Forget, F. Montmessin, T. Navarro, A. Spiga, E. Millour, A. Szantai, and J.-B. Madeleine (2017), Unraveling the Martian water cycle with high-resolution global climate simulations, *Icarus*, *291*, 82–106.
- Rodin, A. V. (2002), On the moment method for the modeling of cloud microphysics in rarefied turbulent atmospheres: I. Condensation and mixing, *Solar System Research*, *36*(2), 97–106, doi:10.1023/A:1015266131539.
- Seele, C., and P. Hartogh (1999), Water vapor of the polar middle atmosphere: Annual variation and summer mesosphere conditions as observed by ground-based microwave spectroscopy, *Geophysical Research Letters*, *26*(11), 1517–1520, doi:10.1029/1999GL900315.
- Shaposhnikov, D. S., A. V. Rodin, and A. S. Medvedev (2016), The water cycle in the general circulation model of the Martian atmosphere, *Solar System Research*, *50*(2), 90–101, doi:10.1134/S0038094616020039.
- Shaposhnikov, D. S., A. V. Rodin, A. S. Medvedev, A. A. Fedorova, T. Kuroda, and P. Hartogh (2018a), Modeling the hydrological cycle in the atmosphere of Mars: Influence of a bimodal size distribution of aerosol nucleation particles, *Journal of Geophysical Research: Planets*, *123*(2), 508–526.
- Shaposhnikov, D. S., A. S. Medvedev, A. V. Rodin, and P. Hartogh (2018b), Seasonal water ”pump” in the atmosphere of Mars: Modeling vertical transport to the thermosphere, doi:10.5281/zenodo.1553514.
- Smith, M. D., M. J. Wolff, R. T. Clancy, and S. L. Murchie (2009), Compact Reconnaissance Imaging Spectrometer observations of water vapor and carbon monoxide, *Journal of Geophysical Research*, *114*(E2), E00D03, doi:10.1029/2008JE003288.
- Trokhimovskiy, A., A. Fedorova, O. Korablev, F. Montmessin, J. L. Bertaux, A. Rodin, and M. D. Smith (2015), Mars’ water vapor mapping by the SPICAM IR spectrometer: Five Martian years of observations, *Icarus*, *251*, 50–64, doi:10.1016/j.icarus.2014.10.007.

Yiğit, E., and A. S. Medvedev (2017), Influence of parameterized small-scale gravity waves on the migrating diurnal tide in Earth's thermosphere, *Journal of Geophysical Research: Space Physics*, *122*(4), 4846–4864, doi:10.1002/2017JA024089.

Water vapor vertical flux

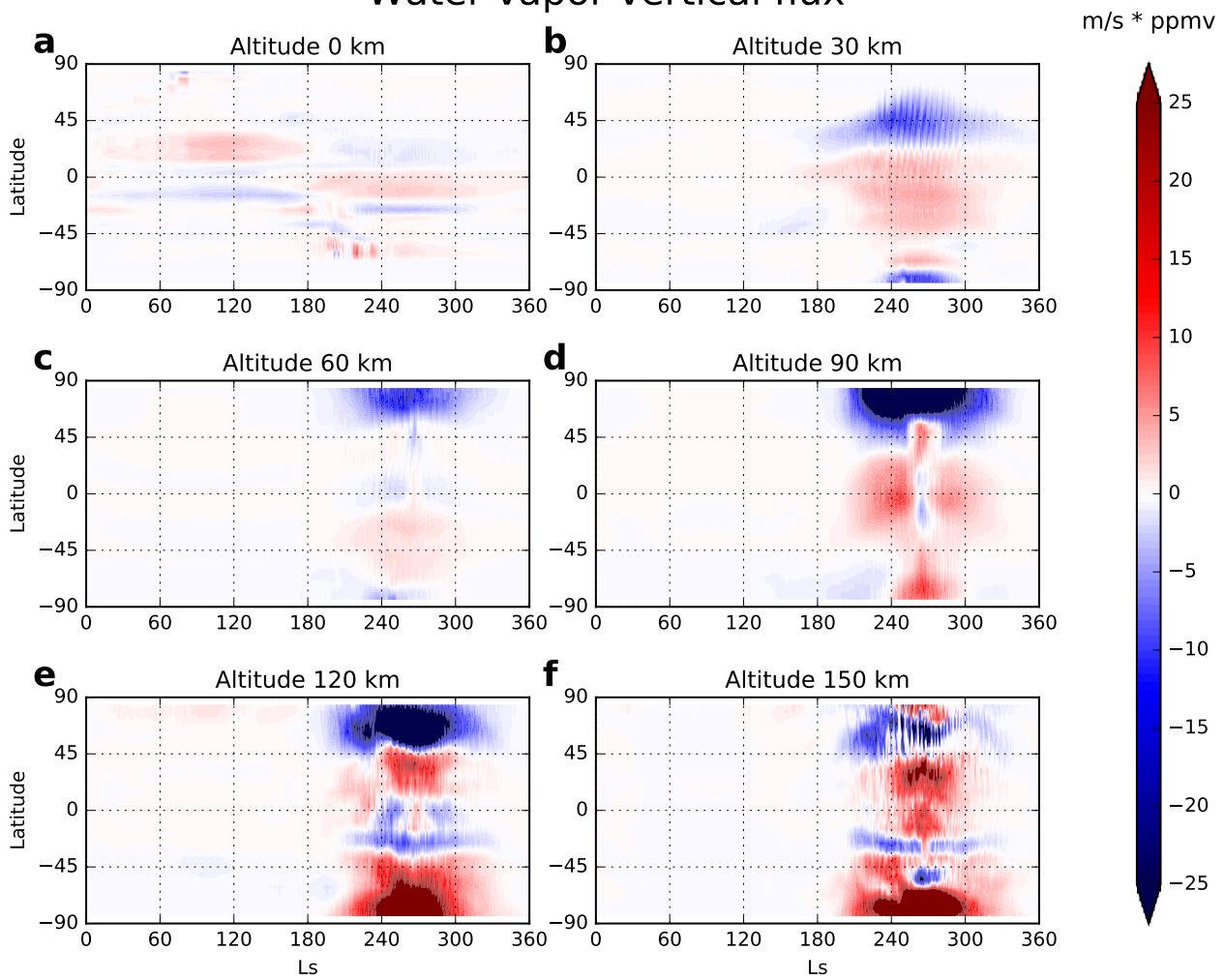


Figure 1. Latitude-seasonal variations of the zonally averaged vertical water vapor flux simulated using the “basic” dust scenario (see section 2) at different altitudes: 0, 30, 60, 90, 120 and 150 km (panels a to f, correspondingly). Positive values (upward fluxes) are plotted in red, negative (downward) fluxes are shown in blue.

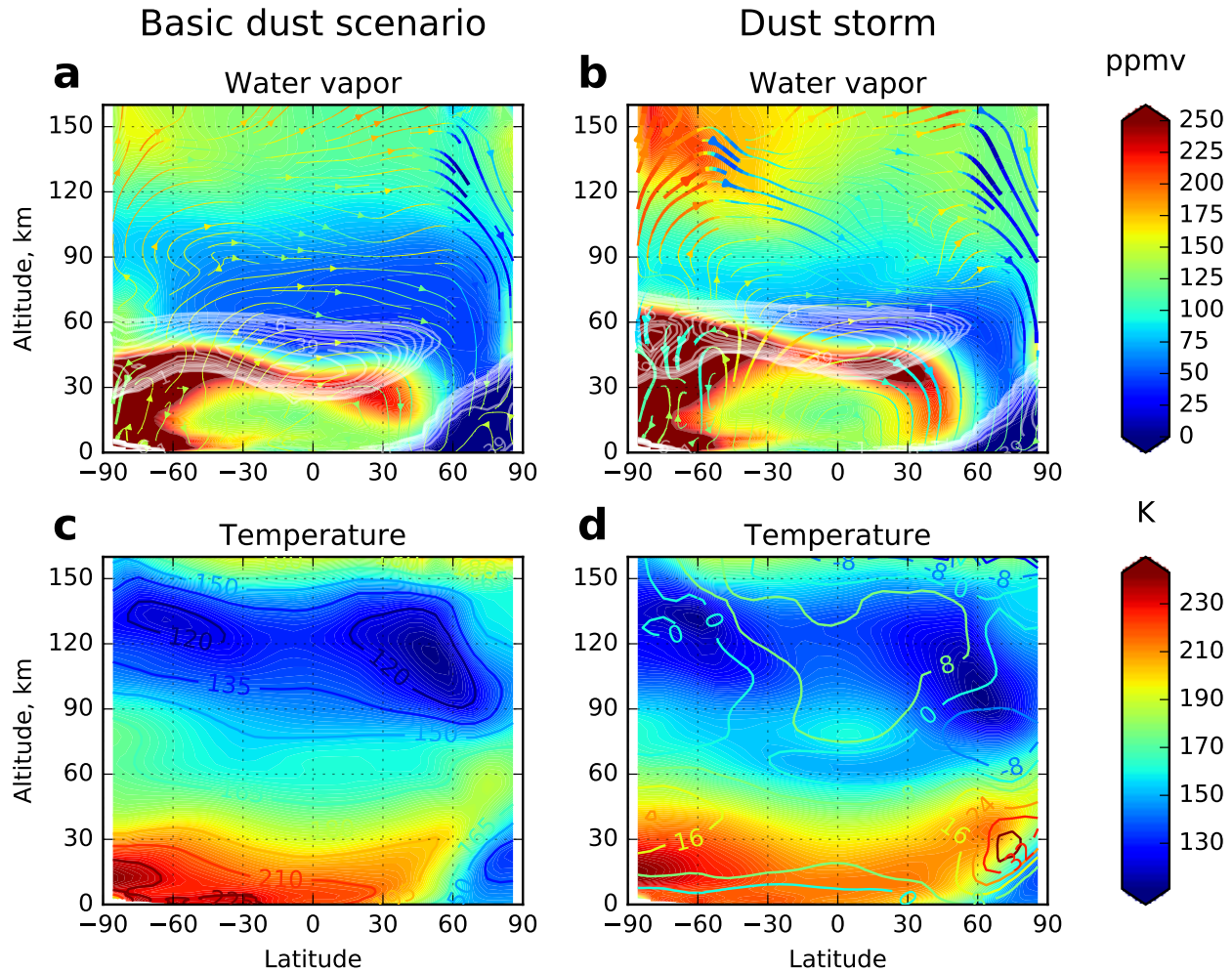


Figure 2. Latitude-altitude cross-sections of the quantities simulated for the “basic” dust scenario (left column) and the MY28 dust storm (right column): (a) Water vapor (shaded), water ice (white contours) and the meridional flux of water vapor (the lines with arrows, the color and thickness of which indicate the vertical direction and magnitude, correspondingly); (b) is the same as in panel (a), but for the dust storm of MY28; (c) temperature (shaded) for the “basic” dust scenario; (d) is the same as in (c), but for the MY28 dust storm scenario, except for the contour lines that show the temperature difference between (d) and (c). All fields are averaged zonally and over the period between $L_s = 250^\circ$ and 270° .

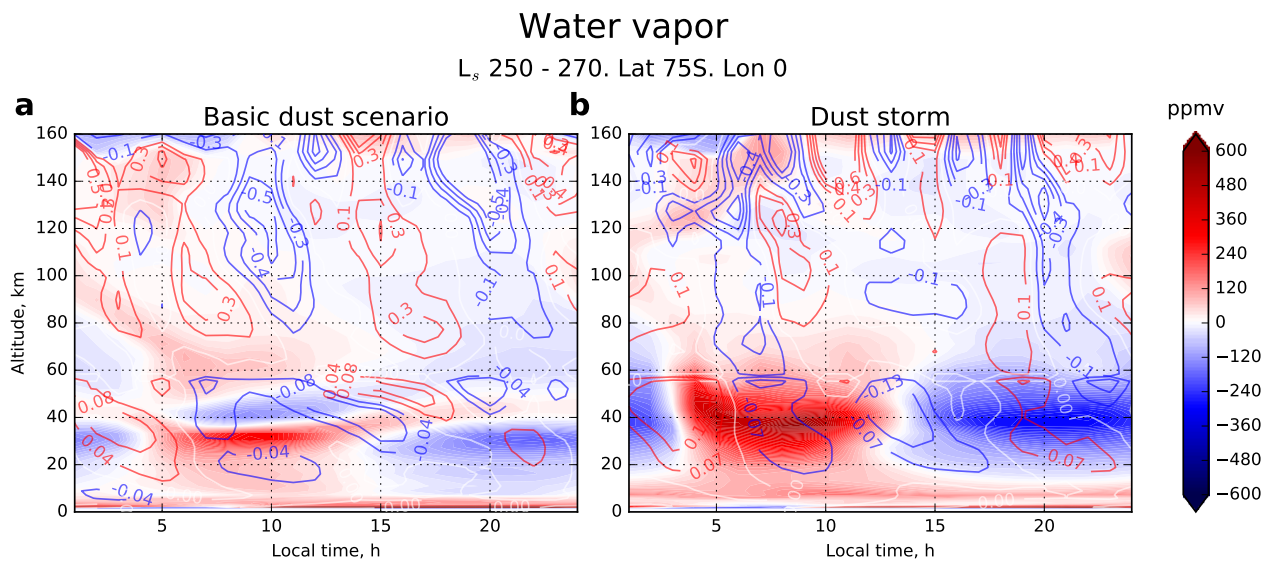


Figure 3. Altitude-local time distributions of deviations from the zonal mean for water vapor (in ppmv, color shades) and vertical velocity (in m s^{-1} , contours). Shown are the composite over the period between $L_s = 250^\circ$ and 270° as functions of local time close to a grid point located near 75°S and 0° longitude. Positive values of the vertical velocity correspond to upward motions. Panel (a) and (b) are for the simulations with the “basic” and “MY28 dust storm” dust scenarios, correspondingly.

Annual water cycle, MY28

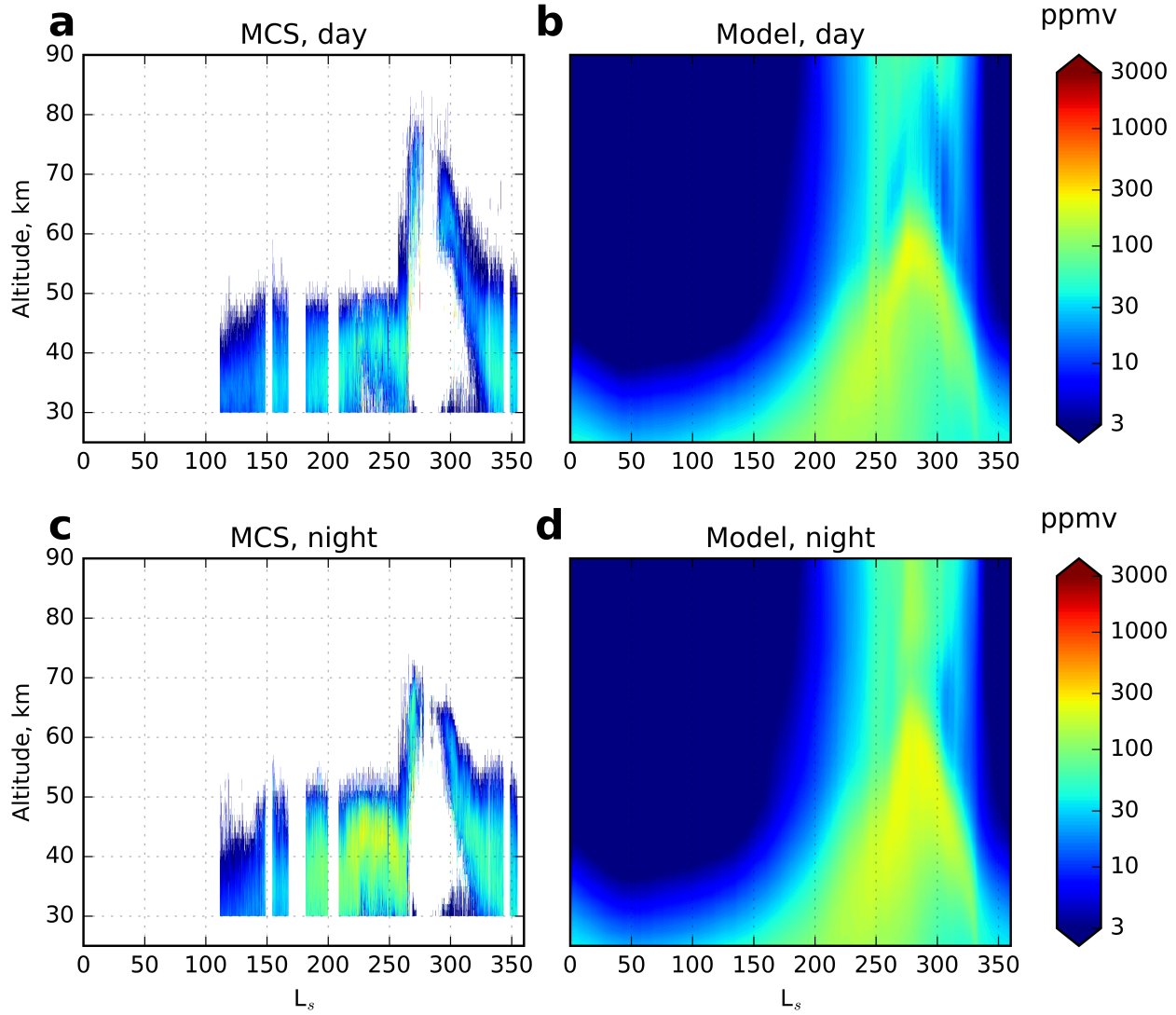


Figure 4. Vertical distribution of the total water (vapor+ice) content derived from the Mars Climate Sounder (MCS) measurements (left column) [Heavens *et al.*, 2018] and simulated with the MPI-MGCM (right column) for the MY28: for the day side ($\sim 15:00$ local time, upper row) and night side (03:00 local time, lower row). In all panels, the values were averaged over longitudes and latitudes. In the simulations, the averaging over 14:00–16:00 and 02:00–04:00 local times was performed.